

Plasma-environment effects on K lines of astrophysical interest

III. IPs, K thresholds, radiative rates, and Auger widths in Fe IX – Fe XVI[★]

J. Deprince¹, M. A. Bautista², S. Fritzsche^{3,4}, J. A. García^{5,6}, T. R. Kallman⁷, C. Mendoza²,
P. Palmeri¹, and P. Quinet^{1,8}

¹ Physique Atomique et Astrophysique, Université de Mons – UMONS, 7000 Mons, Belgium
e-mail: patrick.palmeri@umons.ac.be

² Department of Physics, Western Michigan University, Kalamazoo, MI 49008, USA

³ Helmholtz Institut Jena, 07743 Jena, Germany

⁴ Theoretisch Physikalisches Institut, Friedrich Schiller Universität Jena, 07743 Jena, Germany

⁵ Cahill Center for Astronomy and Astrophysics, California Institute of Technology, Pasadena, CA 91125, USA

⁶ Dr. Karl Remeis-Observatory and Erlangen Centre for Astroparticle Physics, Sternwartstr. 7, 96049 Bamberg, Germany

⁷ NASA Goddard Space Flight Center, Code 662, Greenbelt, MD 20771, USA

⁸ IPNAS, Université de Liège, Sart Tilman, 4000 Liège, Belgium

Received 8 November 2019 / Accepted 29 January 2020

ABSTRACT

Aims. In the context of black-hole accretion disks, we aim to compute the plasma-environment effects on the atomic parameters used to model the decay of K-vacancy states in moderately charged iron ions, namely Fe IX – Fe XVI.

Methods. We used the fully relativistic multiconfiguration Dirac–Fock method approximating the plasma electron–nucleus and electron–electron screenings with a time-averaged Debye–Hückel potential.

Results. We report modified ionization potentials, K-threshold energies, wavelengths, radiative emission rates, and Auger widths for plasmas characterized by electron temperatures and densities in the ranges 10^5 – 10^7 K and 10^{18} – 10^{22} cm⁻³.

Conclusions. This study confirms that the high-resolution X-ray spectrometers onboard the future XRISM and *Athena* space missions will be capable of detecting the lowering of the K edges of these ions due to the extreme plasma conditions occurring in accretion disks around compact objects.

Key words. black hole physics – plasmas – atomic data – X-rays: general

1. Introduction

The present paper is the third in a series devoted to density effects on atomic parameters used to model K-vacancy states in ions of astrophysical interest; namely, ionization potentials, K thresholds, transition wavelengths, radiative emission rates, and Auger widths. Deprince et al. (2019a, hereafter Paper I) computed such data for the oxygen isonuclear sequence and Deprince et al. (2019b, hereafter Paper II) did so for highly ionized Fe ions (Fe XVII – Fe XXV) using the relativistic multiconfiguration Dirac–Fock (MCDF) method (Grant et al. 1980; McKenzie et al. 1980; Grant 1988), as implemented in the GRASP92 (Parpia et al. 1996) and RATIP (Fritzsche 2012) atomic structure packages. The plasma electron–nucleus and electron–electron shielding were approximated with a time-averaged Debye–Hückel (DH) potential. Here we report our calculations using this method for the third-row Fe ions, Fe IX – Fe XVI.

The absorption and emission of high-energy photons occur in the dense plasma (10^{21} – 10^{22} cm⁻³) of the inner region of the accretion disks associated with compact objects, such as black holes and neutron stars. The modeling of the associated X-ray spectra, which can be observed with space telescopes

such as *Chandra*, *XMM-Newton*, *Suzaku*, and *NuSTAR*, gives a measure of the composition, temperature, and degree of ionization for the plasma (Ross & Fabian 2005; García & Kallman 2010). For a black hole, for instance, the distortion of the Fe K lines by the strong relativistic effects constrains its angular momentum (Reynolds 2013; García et al. 2014). However, most of the atomic data used in the modeling of K-shell processes do not take density effects into account, compromising their significance for abundance determinations beyond densities of 10^{18} cm⁻³ (Smith & Brickhouse 2014).

2. Theoretical approach

The MCDF formalism was already described in Paper I and Paper II, so in this paper, we only aim to provide brief indications of the DH modifications that were introduced to handle weakly coupled plasmas. The DH screened Dirac–Coulomb Hamiltonian (Saha & Fritzsche 2006) takes the form of

$$H_{\text{DC}}^{\text{DH}} = \sum_i c\alpha_i \cdot \mathbf{p}_i + \beta_i c^2 - \frac{Z}{r_i} e^{-\mu r_i} + \sum_{i>j} \frac{1}{r_{ij}} e^{-\mu r_{ij}}, \quad (1)$$

where $r_{ij} = |\mathbf{r}_i - \mathbf{r}_j|$ and the plasma screening parameter μ is the inverse of the Debye shielding length λ_D , which can be expressed in atomic units (au) as a function of the plasma electron density n_e and temperature T_e as

[★] Full Tables 4 and 5 are only available at the CDS via anonymous ftp to cdsarc.u-strasbg.fr (130.79.128.5) or via <http://cdsarc.u-strasbg.fr/viz-bin/cat/J/A+A/635/A70>

Table 1. Reference configurations and active orbital sets used to build up the MCDF active space by single and double electron excitations to the corresponding active orbital sets along with the number of configuration state functions (CSFs) generated for the MCDF expansions in Fe IX – Fe XVI.

Ion	Reference configurations	Active orbital set	Number of CSFs
Fe IX	3p ⁶ , [3p]3d, [2p]3d, [1s]3d	{1s, 2s, 2p, 3s, 3p, 3d, 4s}	20009
Fe X	3p ⁵ , [2p]3p ⁶ , [1s]3p ⁶	{1s, 2s, 2p, 3s, 3p, 3d, 4s}	6312
Fe XI	3p ⁴ , [2p]3p ⁵ , [1s]3p ⁵	{1s, 2s, 2p, 3s, 3p, 3d, 4s}	12981
Fe XII	3p ³ , [2p]3p ⁴ , [1s]3p ⁴	{1s, 2s, 2p, 3s, 3p, 3d, 4s}	37967
Fe XIII	3p ² , [2p]3p ³ , [1s]3p ³	{1s, 2s, 2p, 3s, 3p, 3d, 4s}	46771
Fe XIV	3p, [2p]3p ² , [1s]3p ²	{1s, 2s, 2p, 3s, 3p, 3d, 4s}	35109
Fe XV	3s ² , [2p]3s ² 3p, [1s]3s ² 3p	{1s, 2s, 2p, 3s, 3p, 3d, 4s}	16853
Fe XVI	3s, [2p]3s ² , [2p]3s3p, [1s]3s ² , [1s]3s3p	{1s, 2s, 2p, 3s, 3p, 3d, 4s}	25914

Table 2. Computed ionization potentials for Fe IX – Fe XVI as a function of the plasma screening parameter μ (au).

Ion	IP (eV)			
	NIST ^(a)	$\mu = 0.0$	$\mu = 0.1$	$\mu = 0.25$
Fe IX	233.6(4)	230.91	206.99	173.48
Fe X	262.10(12)	263.14	236.65	199.74
Fe XI	290.9(4)	294.15	265.04	224.58
Fe XII	330.8(6)	325.81	294.04	249.75
Fe XIII	361.0(7)	356.95	322.54	274.48
Fe XIV	392.2(7)	388.72	351.68	300.03
Fe XV	456.2(5)	457.14	417.57	362.77
Fe XVI	489.312(14)	488.86	446.68	388.34

Notes. NIST values are also listed for comparison. ^(a)Kramida et al. (2018).

$$\mu = \frac{1}{\lambda_D} = \sqrt{\frac{4\pi n_e}{kT_e}}. \quad (2)$$

Typical plasma conditions in black-hole accretion disks are $T_e \sim 10^5 - 10^7$ K and $n_e \sim 10^{18} - 10^{22}$ cm⁻³ (Schnittman et al. 2013) which, for weakly coupled plasmas correspond to screening parameters of $0.0 \leq \mu \leq 0.24$ au, and, for a completely ionized hydrogen plasma (plasma ionization $Z^* = 1$) correspond to plasma coupling parameters of

$$\Gamma = \frac{e^2}{4\pi\epsilon_0 dkT_e}, \quad (3)$$

with

$$d = \left(\frac{3}{4\pi n_e}\right)^{1/3}, \quad (4)$$

in the range $0.0003 \leq \Gamma \leq 0.3$.

Following Paper II, the MCDF expansions for Fe IX – Fe XVI are generated using the active space method, whereby electrons from the reference configurations in Table 1 are singly and doubly excited to configurations that include $n = 3$ and 4s orbitals. For instance, the non-relativistic configuration [1s2s]3p⁶3d4s, generated by a double electron excitation from the 1s and 2s active subshells of the reference configuration 3p⁶ to the 3d and 4s active orbitals, is included in the expansions of the atomic state functions (ASFs) in Fe IX. As defined in Eq. (1) of Paper II, the number of configuration state functions (CSFs) generated for the MCDF expansions of the ASFs are also given in Table 1 for each ion. We consider plasma screening parameters in the range $0.0 \leq \mu \leq 0.25$ au, the upper-limit choice corresponding to the extreme plasma conditions found in accretion disks.

Table 3. Computed K-thresholds for Fe IX – Fe XVI as a function of the plasma screening parameter μ (au).

Ion	E_K (eV)		
	$\mu = 0.0$	$\mu = 0.1$	$\mu = 0.25$
Fe IX	7308.25	7283.14	7243.32
Fe X	7351.72	7324.04	7280.88
Fe XI	7393.76	7363.48	7316.89
Fe XII	7434.46	7401.52	7351.12
Fe XIII	7483.90	7448.32	7394.27
Fe XIV	7535.85	7497.64	7439.95
Fe XV	7591.60	7550.76	7489.46
Fe XVI	7639.54	7596.05	7531.05

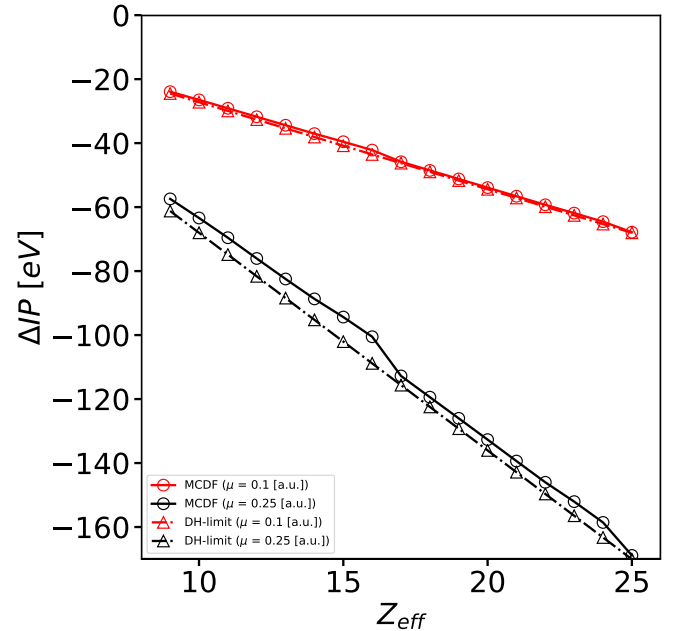


Fig. 1. Ionization potential shifts, ΔIP , in Fe IX – Fe XXV as a function of the effective charge $Z_{\text{eff}} = Z - N + 1$. Red open circles: $\mu = 0.1$ au. Black open circles: $\mu = 0.25$ au. Open triangles: Debye–Hückel limit $\Delta IP_{\text{DH}} = -Z_{\text{eff}} \mu$.

3. Results and discussion

3.1. Ionization potentials and K thresholds

The computed ionization potentials (IPs) and K thresholds (E_K) are given in Tables 2 and 3, respectively, for plasma screening

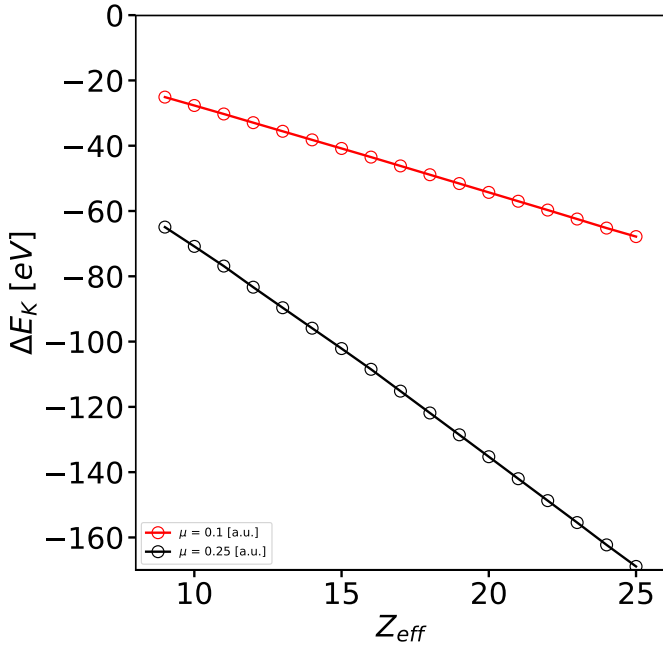


Fig. 2. K-threshold shifts, ΔE_K , in Fe IX – Fe XXV as a function of the effective charge $Z_{\text{eff}} = Z - N + 1$. Red open circles: $\mu = 0.1$ au. Black open circles: $\mu = 0.25$ au.

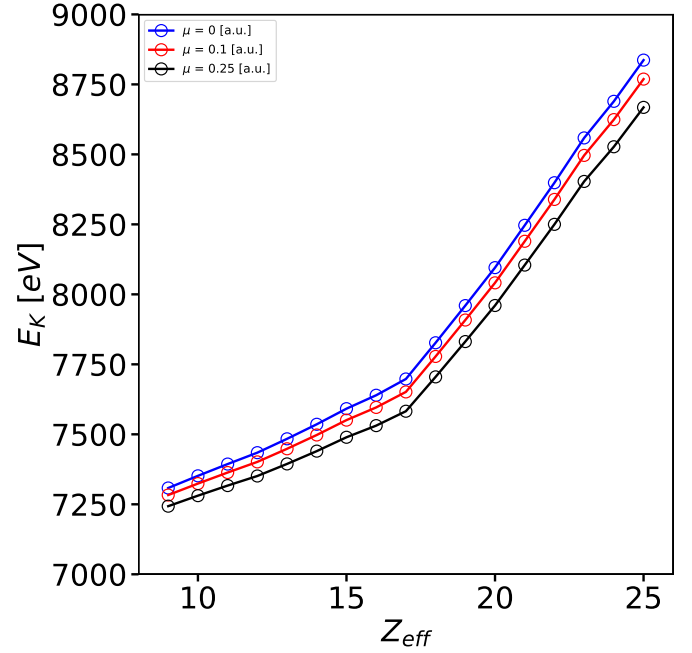


Fig. 4. K thresholds, E_K , in Fe IX – Fe XXV as a function of the effective charge $Z_{\text{eff}} = Z - N + 1$. Blue open circles: $\mu = 0$ au (isolated atom case). Red open circles: $\mu = 0.1$ au. Black open circles: $\mu = 0.25$ au.

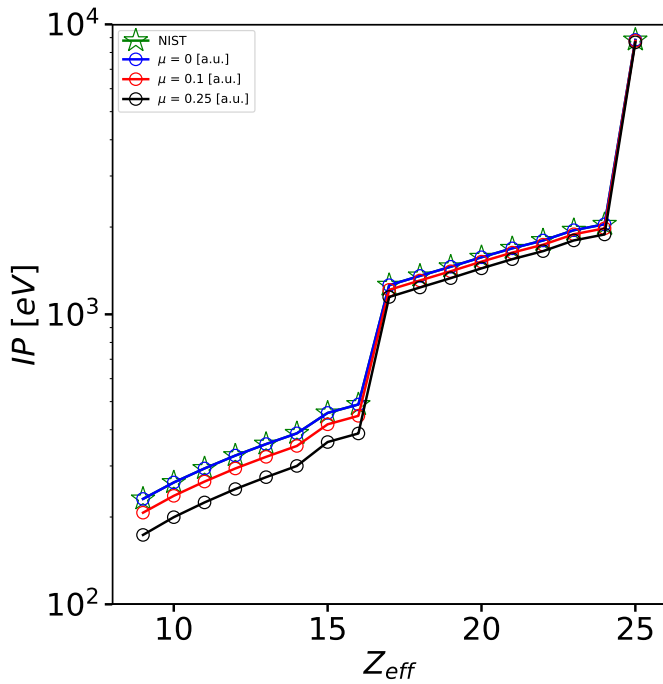


Fig. 3. Ionization potential, IP, in Fe IX – Fe XXV as a function of the effective charge $Z_{\text{eff}} = Z - N + 1$. Blue open circles: $\mu = 0$ au (isolated atom case). Red open circles: $\mu = 0.1$ au. Black open circles: $\mu = 0.25$ au. Green open stars: NIST (Kramida et al. 2018).

parameter $\mu = 0.0, 0.1$ and 0.25 . The case $\mu = 0.1$ corresponds to plasma conditions of $T_e = 10^5$ K and $n_e = 10^{21}$ cm $^{-3}$ and $\mu = 0.25$ au to $T_e = 10^5$ K and $n_e = 10^{22}$ cm $^{-3}$. For the isolated ion case ($\mu = 0.0$ au), the computed IPs are compared in Table 2 with the values quoted in the atomic database (Kramida et al. 2018) at the National Institute of Standards and Technology (NIST), showing an agreement within 0.1%.

Tables 2 and 3 also show the IP and K-threshold lowering by the plasma environment at $\mu = 0.1$ au and $\mu = 0.25$ au:

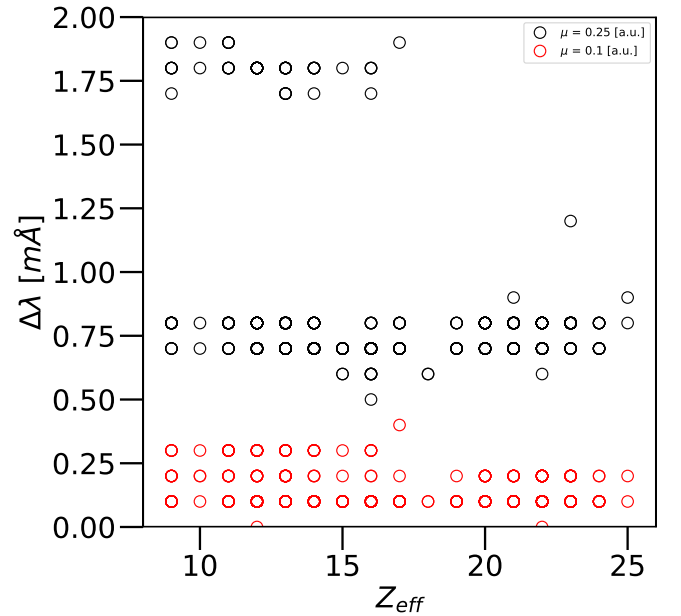


Fig. 5. Wavelength shifts, $\Delta\lambda$, for K lines in Fe IX – Fe XXV as a function of the effective charge $Z_{\text{eff}} = Z - N + 1$. Red circles: $\mu = 0.1$ au. Black circles: $\mu = 0.25$ au.

the IP downshifts are, respectively, 9–10% and 21–25%, while those for the K thresholds, due to their much larger energy, only 0.4–0.6% and 1%. Moreover, in agreement with Paper II, the absolute IP and K-threshold downshifts for each species are practically similar in magnitude. This effect can be further appreciated in Figs. 1 and 2, where we plot the absolute downshifts as a function of the effective charge, $Z_{\text{eff}} = Z - N + 1$ where Z and N are respectively the atomic and electron numbers of the ionic system. We also include in these figures the Fe species with $25 \leq Z_{\text{eff}} \leq 17$ from Paper II and the Debye–Hückel limit $\Delta\text{IP}_{\text{DH}} = -Z_{\text{eff}}\mu$ (Stewart & Pyatt 1966; Crowley 2014).

Table 4. Wavelengths and transition probabilities for the K lines of Fe IX – Fe XVI ($9 \leq Z_{\text{eff}} \leq 16$) computed with plasma screening parameters $\mu = 0.0, 0.1, \text{ and } 0.25 \text{ au}$.

Z_{eff}	Transition	Wavelength (\AA)			Transition probability (s^{-1})		
		$\mu = 0.0$	$\mu = 0.1$	$\mu = 0.25$	$\mu = 0.0$	$\mu = 0.1$	$\mu = 0.25$
9	[1s]3d $^3D_2 - [3p]3d \ ^3F_3$	1.7538	1.7541	1.7556	4.143E+13	4.146E+13	4.164E+13
9	[1s]3d $^3D_1 - [3p]3d \ ^3F_2$	1.7540	1.7542	1.7558	5.446E+13	5.450E+13	5.472E+13
9	[1s]3d $^1D_2 - [3p]3d \ ^3D_3$	1.7546	1.7549	1.7565	1.961E+13	1.958E+13	1.943E+13
9	[1s]3d $^3D_2 - [3p]3d \ ^1D_2$	1.7548	1.7550	1.7566	2.961E+13	2.961E+13	2.961E+13
9	[1s]3d $^1D_2 - [3p]3d \ ^3D_2$	1.7548	1.7551	1.7567	2.518E+13	2.518E+13	2.527E+13
9	[1s]3d $^3D_1 - [3p]3d \ ^3D_1$	1.7549	1.7551	1.7567	2.460E+13	2.464E+13	2.480E+13
9	[1s]3d $^1D_2 - [3p]3d \ ^1F_3$	1.7549	1.7552	1.7567	2.334E+13	2.342E+13	2.381E+13
9	[1s]3d $^1D_2 - [3p]3d \ ^1P_1$	1.7588	1.7590	1.7605	1.556E+13	1.559E+13	1.572E+13
9	[1s]3d $^3D_1 - [2p]3d \ ^3P_0$	1.9357	1.9358	1.9365	6.334E+13	6.332E+13	6.322E+13
9	[1s]3d $^1D_2 - [2p]3d \ ^3P_1$	1.9358	1.9359	1.9366	1.997E+13	1.993E+13	1.973E+13
9	[1s]3d $^3D_1 - [2p]3d \ ^3P_1$	1.9359	1.9360	1.9367	1.061E+14	1.060E+14	1.057E+14
9	[1s]3d $^3D_2 - [2p]3d \ ^3P_1$	1.9359	1.9360	1.9367	3.040E+13	3.044E+13	3.064E+13
9	[1s]3d $^1D_2 - [2p]3d \ ^3P_2$	1.9362	1.9363	1.9370	8.137E+13	8.131E+13	8.098E+13
9	[1s]3d $^3D_1 - [2p]3d \ ^3P_2$	1.9363	1.9364	1.9371	2.921E+13	2.912E+13	2.868E+13
9	[1s]3d $^3D_2 - [2p]3d \ ^3P_2$	1.9363	1.9364	1.9371	3.217E+13	3.221E+13	3.239E+13
9	[1s]3d $^3D_2 - [2p]3d \ ^3F_3$	1.9365	1.9366	1.9372	2.690E+14	2.689E+14	2.684E+13
9	[1s]3d $^1D_2 - [2p]3d \ ^1D_2$	1.9367	1.9368	1.9375	4.062E+13	4.062E+13	4.064E+13
9	[1s]3d $^3D_1 - [2p]3d \ ^1D_2$	1.9368	1.9370	1.9376	1.554E+14	1.554E+14	1.555E+14
9	[1s]3d $^3D_2 - [2p]3d \ ^1D_2$	1.9368	1.9369	1.9376	4.873E+13	4.867E+13	4.837E+13
9	[1s]3d $^1D_2 - [2p]3d \ ^3D_3$	1.9369	1.9370	1.9377	1.297E+14	1.297E+14	1.294E+14
9	[1s]3d $^1D_2 - [2p]3d \ ^3D_1$	1.9381	1.9383	1.9389	6.805E+13	6.799E+13	6.765E+13
9	[1s]3d $^3D_1 - [2p]3d \ ^3D_1$	1.9383	1.9384	1.9390	6.597E+13	6.597E+13	6.598E+13
9	[1s]3d $^3D_1 - [2p]3d \ ^3F_2$	1.9402	1.9403	1.9409	1.280E+14	1.280E+14	1.275E+14
9	[1s]3d $^3D_2 - [2p]3d \ ^3F_2$	1.9402	1.9403	1.9409	1.078E+14	1.077E+14	1.075E+14
9	[1s]3d $^1D_2 - [2p]3d \ ^3D_2$	1.9402	1.9403	1.9410	6.681E+13	6.680E+13	6.675E+13
9	[1s]3d $^1D_2 - [2p]3d \ ^3F_3$	1.9403	1.9404	1.9411	1.367E+14	1.366E+14	1.364E+14
9	[1s]3d $^1D_2 - [2p]3d \ ^1P_1$	1.9419	1.9420	1.9427	2.439E+13	2.446E+13	2.479E+13
9	[1s]3d $^3D_1 - [2p]3d \ ^1P_1$	1.9420	1.9421	1.9428	1.776E+13	1.776E+13	1.775E+13
9	[1s]3d $^3D_2 - [2p]3d \ ^1P_1$	1.9420	1.9421	1.9428	7.565E+13	7.555E+13	7.503E+13
10	[1s]3p $^6 \ ^2S_{1/2} - 3p^5 \ ^2P_{3/2}$	1.7519	1.7521	1.7537	7.603E+13	7.610E+13	7.647E+13
10	[1s]3p $^6 \ ^2S_{1/2} - 3p^5 \ ^2P_{1/2}$	1.7523	1.7526	1.7542	3.677E+13	3.681E+13	3.698E+13
10	[1s]3p $^6 \ ^2S_{1/2} - [2p]3p^6 \ ^2P_{3/2}$	1.9367	1.9369	1.9375	3.830E+14	3.828E+14	3.822E+14
10	[1s]3p $^6 \ ^2S_{1/2} - [2p]3p^6 \ ^2P_{1/2}$	1.9405	1.9406	1.9412	1.880E+14	1.880E+14	1.877E+14

Notes. Data obtained with $\mu = 0 \text{ au}$ correspond to the isolated atom. A complete version of this table is available in electronic form from the CDS.

The linear lowerings of both the IP and K threshold, ΔIP and ΔE_K , respectively, with Z_{eff} and their close magnitude for each ion are hereby reiterated. We also verify that the Debye–Hückel limit is a good approximation of the IP lowering except for two discontinuities at $Z_{\text{eff}} = 17$ and 25 conspicuous at the higher plasma screening parameter ($\mu = 0.25$), which are caused respectively by the closing of the L and K shells. It can be seen in Fig. 3 that the IP increases linearly with Z_{eff} but two large escalations, namely a factor of 2.6 and 4, occur respectively for the closed L- and K-shell species Fe XVII and Fe XXV. The behavior of the K threshold with effective charge is somewhat different (see Fig. 4); although it still increases linearly, the gradient becomes steeper at $Z_{\text{eff}} = 17$ and no effect is appreciable at $Z_{\text{eff}} = 25$ since the K-shell electron is located deeper close to the nucleus in contrast to the relatively weakly bound valence electron.

3.2. Radiative transitions

The present MCDF K-line wavelengths are in excellent agreement with those obtained with the pseudo-relativistic

Hartree–Fock (HFR) method by Palmeri et al. (2003) and Mendoza et al. (2004), differing on average by less than 0.1%, and the dispersion of the radiative transition probabilities is not larger than 20%. Regarding plasma effects, in Table 4, we tabulate the wavelengths and A-values for the stronger K lines ($A_{ki} \geq 10^{13} \text{ s}^{-1}$) at $\mu = 0, 0.1, \text{ and } 0.25 \text{ au}$, where it can be seen that they are hardly modified redshifted by $\sim 1\text{--}2 \text{ m\AA}$ or less and the radiative rates only vary by a few percent in most cases (15–20% in a handful of transitions).

In Fig. 5, we plot the wavelength shifts as a function of the ionic effective charge $9 \leq Z_{\text{eff}} \leq 25$ for $\mu = 0.1$ and 0.25 au, again including the data from Paper II for Fe XVII – Fe XXV. We do not see a well-defined trend with Z_{eff} , but for $Z_{\text{eff}} \leq 17$, the $K\beta$ redshifts at $\mu = 0.25 \text{ au}$ are found to be $\sim 2 \text{ m\AA}$; that is, a factor of 2 larger than the $K\alpha$ lines.

3.3. Auger widths

The Auger widths for the K-vacancy states we computed for the isolated atom are in good agreement with those obtained

Table 5. Plasma environment effects on the Auger widths of K-vacancy states in Fe IX – Fe XVI ($9 \leq Z_{\text{eff}} \leq 16$) computed with plasma screening parameters $\mu = 0.0, 0.1, \text{ and } 0.25 \text{ au}$.

Z_{eff}	Level	Auger width (s^{-1})		
		$\mu = 0.0$	$\mu = 0.1$	$\mu = 0.25$
9	[1s]3d $^3\text{D}_1$	1.057E+15	1.054E+15	1.051E+15
9	[1s]3d $^3\text{D}_2$	1.056E+15	1.053E+15	1.050E+15
9	[1s]3d $^3\text{D}_3$	1.056E+15	1.053E+15	1.050E+15
9	[1s]3d $^1\text{D}_2$	1.056E+15	1.053E+15	1.050E+15
10	[1s]3p 6 $^2\text{S}_{1/2}$	9.832E+14	9.789E+14	9.747E+14
11	[1s]3p 5 $^3\text{P}_2$	1.252E+15	1.244E+15	1.230E+15
11	[1s]3p 5 $^3\text{P}_1$	1.251E+15	1.243E+15	1.230E+15
11	[1s]3p 5 $^3\text{P}_0$	1.254E+15	1.246E+15	1.232E+15
11	[1s]3p 5 $^1\text{P}_1$	1.235E+15	1.227E+15	1.213E+15
12	[1s]3p 4 $^4\text{P}_{5/2}$	1.257E+15	1.254E+15	1.247E+15
12	[1s]3p 4 $^4\text{P}_{3/2}$	1.256E+15	1.254E+15	1.246E+15
12	[1s]3p 4 $^4\text{P}_{1/2}$	1.259E+15	1.256E+15	1.248E+15
12	[1s]3p 4 $^2\text{P}_{3/2}$	1.231E+15	1.228E+15	1.220E+15
12	[1s]3p 4 $^2\text{P}_{1/2}$	1.226E+15	1.224E+15	1.216E+15
12	[1s]3p 4 $^2\text{D}_{5/2}$	1.248E+15	1.246E+15	1.238E+15
12	[1s]3p 4 $^2\text{D}_{3/2}$	1.247E+15	1.244E+15	1.237E+15
12	[1s]3p 4 $^2\text{S}_{1/2}$	1.247E+15	1.244E+15	1.237E+15

Notes. Data obtained with $\mu = 0 \text{ au}$ correspond to the isolated atom. A complete version of this table is available in electronic form from the CDS.

by Palmeri et al. (2003) and Mendoza et al. (2004), differences being no large than 10–15%. Similarly to the radiative rates, our Auger widths are only weakly modified by the plasma environment (see Table 5), with the reductions at $\mu = 0.25 \text{ au}$ no greater than a few percent (<3%) with respect to the isolated atom.

4. Summary and conclusions

Following our previous work on the oxygen isonuclear sequence (Paper I) and on the highly charged iron ions (Paper II), we studied the influence of the plasma environment on the atomic structure and on the radiative and Auger parameters associated with the K lines of the moderately charged species Fe IX – Fe XVI. The IPs, K-thresholds, wavelengths, radiative transition probabilities, and Auger widths have been calculated with the MCDF method, which includes a Debye–Hückel potential to model the plasma screening effects. To simulate the plasma conditions in compact-object accretion disks, we varied the plasma screening parameter μ from 0 au to 0.25 au. Our main results are summarized as follows.

1. We confirmed the linear redshifts of both the IP and K threshold with the effective ionic charge and their close magnitude for each species. Their values range between -20 eV to -100 eV .
2. The radiative and Auger rates are only marginally modified by the plasma environment (by a few percent overall).
3. The transition wavelengths are redshifted by less than 1 m\AA , but for the most extreme conditions studied ($\mu = 0.25 \text{ au}$), the more sensitive $\text{K}\beta$ lines are shifted to the red by about -2 m\AA .

As discussed in the context of the highly ionized Fe ions (Paper II), the high-density plasma effects presented here are expected to have a noticeable impact on the modeling of astrophysical environments where the temperature and density reach

high enough values. A prime example is the material in accretion disks formed around compact objects such as white dwarfs, neutron stars, and black holes. The standard α -disk model (Shakura & Sunyaev 1973) predicts densities in the mid-plane of the disk of order $\sim 10^{13} - 10^{27} \text{ cm}^{-3}$ for black holes with masses in the range $10 - 10^9 M_{\odot}$ and reasonable values of the accretion rate and viscosity. Recent simulations based on general relativity and magnetic hydrodynamics tend to agree with the orders of magnitude of these predictions, with lower mass objects having larger densities (e.g., Schnittman et al. 2013; Jiang et al. 2019a). Accreting black holes are observed to typically emit large amounts of X-rays with a fraction of this flux reprocessed in the disk itself. This reprocessing produces a rich spectrum of fluorescence lines and other atomic features commonly described as the X-ray reflection spectrum (Ross & Fabian 2005; García & Kallman 2010). The ubiquitously of these signatures has made X-ray reflection spectroscopy a common and powerful technique for obtaining physical information regarding the composition and ionization state of the accretion flow and the coveted black-hole spin (Fabian et al. 1989; Reynolds 2019). Due to their abundance and comparatively large fluorescence yield, along with their crucial role in determining the ionization structure of the gas producing most of the reprocessed signal, the iron ionic species featured in this paper are of particular interest for reflection modeling (García et al. 2013).

The high-quality observational data available in the last decade have revealed a number of important issues in the spectral modeling of accreting black holes; for instance, the modeling of the so-called “soft excess” in the spectrum active galactic nuclei (AGN). This is a broad and featureless component observed at soft X-ray energies ($\sim 1 \text{ keV}$), which can also be described as such by several physically distinct models. As was recently demonstrated for the Seyfert 1 AGN Mrk 509 (García et al. 2019), one such model is based on the X-ray reflection spectrum from a very dense accretion disk. Higher disk densities lead to a strong excess of the reflected continuum at soft energies due to the enhancement of free–free heating in the atmosphere of the disk, which increases with rising density (Ballantyne 2004; García et al. 2016). An extended study of 17 AGN characterized by a strong soft excess have made use of high-density reflection models to reproduce their X-ray spectra (Jiang et al. 2019b), finding tentative correlations between the black-hole mass, accretion rate, and accretion-disk density.

In the study of accreting sources, the nominal values of some of the parameters obtained in reflection modeling are also relevant: in particular, the iron abundance is commonly found to be larger than the expected Solar value by factors of two up to ten (García et al. 2018). This trend is found in accreting black holes with very different masses suggesting an artificial origin rather than a physical overabundance. Reflection calculations at densities higher than the traditionally assumed values ($\sim 10^{15} \text{ cm}^{-3}$) have shown promise in addressing both issues. Recent analyses of the reflection spectra from AGN and black-hole binaries (BHB) appear to indicate that the high-density effects are acting positively to resolve the mystery of the high iron abundances leading to substantially lower observed values (Tomsick et al. 2018; Jiang et al. 2019b,c).

The plasma environment effects presented here have not yet been included in the studies described above. However, they are expected to affect further the atomic features imprinted in the reflection spectra and, consequently, to modify the quantities deduced from the fits. Even though a comprehensive analysis of the propagation of plasma effects in synthetic spectra is outside the scope of the present work, our conclusions suggest that some

of the spectral profiles observed in the X-ray reflected spectrum from accreting sources may be modified to an extent that could potentially influence their characterization. This will be relevant for the next generation of X-ray observatories such as XRISM (Tashiro et al. 2018) and *Athena* (Nandra et al. 2013), which will provide an enhanced effective area in the X-ray band and instrumentation with far superior spectral resolution (of the order of a few eV) to aid in the detection of the lowering of the ionic K edges in extreme plasma conditions.

Acknowledgements. JD is Research Fellow of the Belgian Fund for Research Training in Industry and Agriculture (FRIA) while PP and PQ are, respectively, Research Associate and Research Director of the Belgian Fund for Scientific Research (F.R.S.-FNRS). Financial supports from these organizations, as well as from the NASA Astrophysics Research and Analysis Program (grant 80NSSC17K0345) are gratefully acknowledged. JAG acknowledges support from the Alexander von Humboldt Foundation.

References

- Ballantyne, D. R. 2004, *MNRAS*, 351, 57
- Crowley, B. J. B. 2014, *High Energy Dens. Phys.*, 13, 84
- Deprince, J., Bautista, M. A., Fritzsche, S., et al. 2019a, *A&A*, 624, A74
- Deprince, J., Bautista, M. A., Fritzsche, S., et al. 2019b, *A&A*, 626, A83
- Fabian, A. C., Rees, M. J., Stella, L., & White, N. E. 1989, *MNRAS*, 238, 729
- Fritzsche, S. 2012, *Comput. Phys. Commun.*, 183, 1523
- García, J., & Kallman, T. R. 2010, *ApJ*, 718, 695
- García, J., Dauser, T., Reynolds, C. S., et al. 2013, *ApJ*, 768, 146
- García, J., Dauser, T., Lohfink, A., et al. 2014, *ApJ*, 782, 76
- García, J. A., Grinberg, V., Steiner, J. F., et al. 2016, *ApJ*, 819, 76
- García, J. A., Kallman, T. R., Bautista, M., et al. 2018, *ASP Conf. Ser.*, 515, 282
- García, J. A., Kara, E., Walton, D., et al. 2019, *ApJ*, 871, 88
- Grant, I. P. 1988, *Comput. Chem.*, 2, 1
- Grant, I. P., McKenzie, B. J., Norrington, P. H., Mayers, D. F., & Pyper, N. C. 1980, *Comput. Phys. Commun.*, 21, 207
- Jiang, Y.-F., Blaes, O., Stone, J. M., & Davis, S. W. 2019a, *ApJ*, 885, 144
- Jiang, J., Fabian, A. C., Dauer, T., et al. 2019b, *MNRAS*, 489, 3436
- Jiang, J., Fabian, A. C., Wang, J., et al. 2019c, *MNRAS*, 484, 1972
- Kramida, A., Ralchenko, Yu., Reader, J., & NIST ASD Team 2018, *NIST Atomic Spectra Database (version 5.6.1)*. Available: <http://physics.nist.gov/asd> [2019, February 1]. National Institute of Standards and Technology, Gaithersburg, MD
- McKenzie, B. J., Grant, I. P., & Norrington, P. H. 1980, *Comput. Phys. Commun.*, 21, 233
- Mendoza, C., Kallman, T. R., Bautista, M. A., & Palmeri, P. 2004, *A&A*, 414, 377
- Nandra, K., Barret, D., Barcons, X., et al. 2013, ArXiv e-prints [arXiv:1306.2307]
- Palmeri, P., Mendoza, C., Kallman, T. R., Bautista, M. A., & Meléndez, M. 2003, *A&A*, 410, 359
- Parpia, F. A., Fischer, C. F., & Grant, I. P. 1996, *Comput. Phys. Commun.*, 94, 249
- Reynolds, C. S. 2013, *Classical Quantum Gravity*, 30, 244004
- Reynolds, C. S. 2019, *Nat. Astron.*, 3, 41
- Ross, R. R., & Fabian, A. C. 2005, *MNRAS*, 358, 211
- Saha, B., & Fritzsche, S. 2006, *Phys. Rev. E*, 73, 036405
- Schnittman, J. D., Krolik, J. H., & Noble, S. C. 2013, *ApJ*, 769, 156
- Shakura, N. I., & Sunyaev, R. A. 1973, *A&A*, 24, 337
- Smith, R. K., & Brickhouse, N. S. 2014, *Adv. At. Mol. Opt. Phys.*, 63, 271
- Stewart, J. C., & Pyatt, Jr., K. D. 1966, *ApJ*, 144, 1203
- Tashiro, M., Maejima, H., Toda, K., et al. 2018, *SPIE Conf. Ser.*, 10699, 1069922
- Tomsick, J. A., Parker, M. L., García, J. A., et al. 2018, *ApJ*, 855, 3